



RESEARCH ARTICLE

10.1002/2014JE004618

Special Section:

Results from the first 360 Sols of the Mars Science Laboratory Mission: Bradbury Landing through Yellowknife Bay

Key Points:

- We calculate the thermal inertia and surface energy budget at Gale Crater
- We use MSL REMS measurements for our calculations

Correspondence to:

G. M. Martínez, gemartin@umich.edu

Citation:

Martínez, G. M., et al. (2014), Surface energy budget and thermal inertia at Gale Crater: Calculations from ground-based measurements, *J. Geophys. Res. Planets*, 119, 1822–1838, doi:10.1002/2014JE004618.

Received 31 JAN 2014

Accepted 12 JUL 2014

Accepted article online 17 JUL 2014

Published online 8 AUG 2014

Surface energy budget and thermal inertia at Gale Crater: Calculations from ground-based measurements

G. M. Martínez¹, N. Rennó¹, E. Fischer¹, C. S. Borlina¹, B. Hallet², M. de la Torre Juárez³, A. R. Vasavada³, M. Ramos⁴, V. Hamilton⁵, J. Gomez-Elvira⁶, and R. M. Haberle⁷

¹Department of Atmospheric, Oceanic and Space Sciences, University of Michigan, Ann Arbor, Michigan, USA, ²Department of Earth and Space Sciences, University of Washington, Seattle, Washington, USA, ³Jet Propulsion Laboratory, Pasadena, California, USA, ⁴Departamento de Física, Universidad de Alcalá de Henares, Madrid, Spain, ⁵Department of Space Studies, Southwest Research Institute, Boulder, Colorado, USA, ⁶Centro de Astrobiología, Madrid, Spain, ⁷Space Science Division, NASA Ames Research Center, Moffett Field, California, USA

Abstract The analysis of the surface energy budget (SEB) yields insights into soil-atmosphere interactions and local climates, while the analysis of the thermal inertia (*I*) of shallow subsurfaces provides context for evaluating geological features. Mars orbital data have been used to determine thermal inertias at horizontal scales of $\sim 10^4$ m² to $\sim 10^7$ m². Here we use measurements of ground temperature and atmospheric variables by Curiosity to calculate thermal inertias at Gale Crater at horizontal scales of $\sim 10^2$ m². We analyze three sols representing distinct environmental conditions and soil properties, sol 82 at Rocknest (RCK), sol 112 at Point Lake (PL), and sol 139 at Yellowknife Bay (YKB). Our results indicate that the largest thermal inertia $I = 452 \text{ J m}^{-2} \text{ K}^{-1} \text{ s}^{-1/2}$ (SI units used throughout this article) is found at YKB followed by PL with $I = 306$ and RCK with $I = 295$. These values are consistent with the expected thermal inertias for the types of terrain imaged by Mastcam and with previous satellite estimations at Gale Crater. We also calculate the SEB using data from measurements by Curiosity's Rover Environmental Monitoring Station and dust opacity values derived from measurements by Mastcam. The knowledge of the SEB and thermal inertia has the potential to enhance our understanding of the climate, the geology, and the habitability of Mars.

1. Introduction

The heat flux into the surface and the shallow subsurface determines the near-surface thermal environment and therefore constrains the habitability of Mars. The flux of radiation reaching the surface might constrain the existence of microbial habitats on the surface and shallow subsurface of Mars [Cockell and Raven, 2004], while the temperature of the soil constrains its water content and the formation of liquid brines and interfacial water, the most likely forms of liquid water on Mars [e.g., Martínez and Rennó, 2013]. In addition, weathering and erosion of the Martian surface is driven by the amount of energy available for wind erosion [Sullivan et al., 2005], for inducing thermal stresses in exposed rocks and bedrock, and for enabling diverse aqueous processes to weather rock [Golombek et al., 2012].

The total amount of energy at the surface available for conduction in the soil (*G*) is determined by the surface energy budget (SEB), that is,

$$G = Q_{SW}(1 - \alpha) + Q_{LW} - \sigma \epsilon T_g^4 - Q_H - Q_E, \tag{1}$$

where Q_{SW} is the downwelling shortwave (SW) solar radiation, α is the surface albedo, Q_{LW} is the downwelling longwave (LW) radiation flux from the atmosphere, $\sigma \epsilon T_g^4$ is the surface upwelling longwave radiation flux, ϵ is the surface emissivity, $\sigma = 5.670 \times 10^{-8} \text{ W m}^{-2} \text{ K}^{-4}$ is the Stefan Boltzmann constant, T_g is the ground temperature, Q_H is the sensible heat flux, and Q_E is the latent heat flux. Upward fluxes are defined as negative (cooling) while downward fluxes are defined as positive (heating). The first two terms on the right of equation (1) make up the (radiative) forcing of the surface, whereas the third, fourth, and fifth terms are considered to be the responses to this forcing. The forcing terms depend on the distance to the sun, the surface albedo, and the atmospheric opacity, while the response terms depend on the physical properties of the soil. In fact, they depend strongly on the thermal inertia of the soil.

This is an open access article under the terms of the Creative Commons Attribution-NonCommercial-NoDerivs License, which permits use and distribution in any medium, provided the original work is properly cited, the use is non-commercial and no modifications or adaptations are made.

The ability of the soil to exchange the radiative energy received at the surface with the shallow subsurface and the near-surface air depends, among other factors, on the thermal inertia of the soil. Given a radiative forcing at the surface, the thermal inertia regulates thermal excursions of ground and subsurface temperatures at diurnal and seasonal timescales. It also controls the temperature of the near-surface air by constraining turbulent convection.

The thermal inertia of the soil is defined as

$$I = \sqrt{\lambda \rho c_p}, \quad (2)$$

where λ is the thermal conductivity of the soil, ρ the soil density, and c_p the soil specific heat. The thermal inertia depends on a complex combination of particle size, rock abundance, exposure of bedrock, and degree of induration [Presley and Christensen, 1997; Mellon et al., 2000; Fergason et al., 2006a; Piqueux and Christensen, 2009a, 2009b].

Previous studies used numerical models to calculate and assess the significance of the various terms of the Martian SEB budget described in equation (1). The standard procedure used is to tune a column model to match in situ measurements of air temperature and wind speed. Once the results of the simulations match the measurements, the various terms of the SEB are estimated. The model is tuned by adjusting the value of parameters like albedo, thermal inertia, and dust opacity. Following this procedure, Sutton et al. [1978] and Haberle et al. [1993] calculated the sensible heat flux Q_H at the Viking landing sites, while Savijärvi [1999] and Savijärvi and Määttänen [2010] determined the various terms of the SEB at the Mars Pathfinder and Phoenix landing sites. Using an alternative approach that considers in situ air temperatures measured at different heights and the Monin-Obukhov similarity theory, Davy et al. [2010] calculated Q_H at the Phoenix landing site.

Three distinct approaches have been used to calculate the thermal inertia of the Martian surface. The first is to fit a model of the diurnal variation of temperature to the surface brightness temperature measured continuously over a certain period of the day using telescopes or spacecraft [Sinton and Strong, 1960; Kieffer et al., 1977]. In this case, the albedo and the thermal inertia are adjusted to fit the observations. A second method was developed more recently to analyze single-point surface temperature measurements by the Thermal Emission Spectrometer (TES) on board the Mars Global Surveyor [Mellon et al., 2000]. In this case, a seven-dimensional lookup table with values of parameters such as albedo, thermal inertia, surface pressure, dust opacity, latitude, longitude, and time of day is produced using thermal models [Haberle and Jakosky, 1991]. Latitude, longitude, time of day, and season are obtained from the spacecraft mission logs, while albedo, surface pressure and dust opacity are obtained from TES measurements. Then, the lookup table is used to determine the value of thermal inertia at the specific location, season, and time of the day being studied. This second approach has also been used to calculate values of the thermal inertia using data from the Thermal Emission Imaging System (THEMIS) and Observatoire pour la Mineralogie, l'Eau, les Glaces et l'Activite (OMEGA) observations [Fergason et al., 2006a; Fergason et al., 2012; Gondet et al., 2013]. Finally, a third approach has been used by Fergason et al. [2006b] and Hamilton et al. [2014]. They obtained the thermal inertia at the Mars Exploration Rover (MER) and Mars Science Laboratory (MSL) landing sites also using thermal models [Kieffer, 2013], but they fitted the results of the model calculations to ground-based soil temperatures measured by the Miniature Thermal Emission Spectrometer (Mini-TES) and the Rover Environmental Station (REMS) throughout the day.

The global coverage of orbiters has allowed the mapping of the thermal inertia of most of the Martian surface. This has contributed to our understanding of surface geology and climate and has supported landing site selection [Putzig and Mellon, 2007; Fergason et al., 2012]. This global mapping has been performed using either bolometric temperatures accounting for atmospheric effects or surface kinetic temperatures derived from spectral measurements with spatial resolutions ranging from $\sim 10^7 \text{ m}^2$ (using TES measurements) to $\sim 10^4 \text{ m}^2$ (using THEMIS measurements) and with temporal resolutions of one measurement per day [Mellon et al., 2000; Christensen et al., 2001, 2004b; Putzig et al., 2005; Fergason et al., 2012]. Due to their spatial and temporal coverage, surface temperature measurements by satellite are affected by surface heterogeneities, which range horizontally within the sensor footprint, and vertically from a few decimeters to a few meters of depth (the seasonal thermal skin depth) [Putzig and Mellon, 2007]. Therefore, whenever horizontal mixtures or near-surface layers of differing materials are present, the values of the thermal inertia derived from orbiters may change with time of day and season, providing information about the scale of the heterogeneity.

Here we complement numerical modeling and satellite observations by calculating the SEB and thermal inertia using ground temperature measurements made by Curiosity at high spatial ($\sim 100 \text{ m}^2$) and temporal

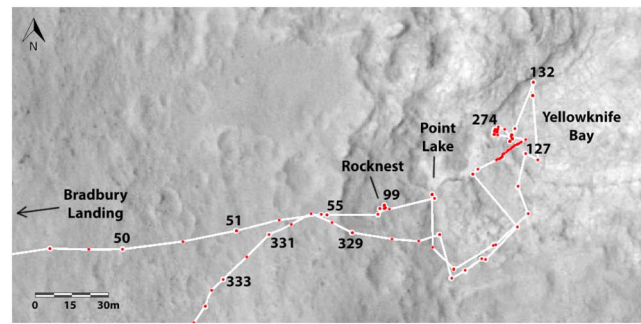


Figure 1. Partial traverse map of the MSL rover in Gale Crater (137.4°E, -4.6°N) with sol numbers and points of interest.

thermal inertia. In particular, REMS is a suite of sensors aimed at studying the environmental conditions along the rover traverse [Gómez-Elvira *et al.*, 2012]. REMS is measuring UV radiation flux at the Martian surface for the first time. In addition, REMS is enhancing significantly our knowledge of ground temperature variations on Mars. This type of data set was pioneered by the Mini-TES aboard the MERs [Spanovich *et al.*, 2006], but the REMS ground temperature sensor (GTS) is providing more continuous and systematic measurements than done before. In addition, REMS is measuring atmospheric pressure, relative humidity, atmospheric temperature, and wind speed [Gómez-Elvira *et al.*, 2012].

Studies of thermal inertia from ground-based measurements are of paramount importance because information about the shallow subsurface is lacking. A rover traversing nearly horizontal sedimentary rocks would acquire limited data of the near-subsurface environment. Subsurface sensing could be correlated with local outcrops and traced laterally, providing a broader knowledge of the local geology. Therefore, techniques that sense subsurface structural continuity such as the thermal inertia of the shallow subsurface could provide contextual information for other measurements [Zorzano and Vázquez, 2006; Bandfield and Feldman, 2008; Mellon *et al.*, 2008; Vasavada *et al.*, 2012], complementary to that obtained by cameras and contact instruments.

Here we analyze the data obtained in three different locations in Gale Crater (Figure 1), Rocknest (RCK), Point Lake (PL), and Yellowknife Bay (YKB). As explained in section 2, we chose these areas because the rover was stationary and the environmental conditions and soil properties of these sites were distinct from each other, making their study particularly interesting.

In section 2, we describe the REMS data products used in this study, focusing on ground temperature data. In section 3, we explain how the different terms of the SEB described in equation (1) are determined from REMS measurements. Then, we develop the method to calculate the thermal inertia and compare its results with that of other approaches. In section 4, we show the calculated SEB and determine the relative significance of various terms. Then we present values of thermal inertia obtained for each study site. In section 5, we describe uncertainties and sources of error. In section 6, we summarize our results and discuss their significance.

2. REMS Environmental Sensor Suite

REMS was developed to assess the environmental conditions along Curiosity's traverse in Gale Crater. REMS has been measuring atmospheric pressure, atmospheric relative humidity, ground and atmospheric temperatures, UV radiation fluxes, and horizontal wind speeds [Gómez-Elvira *et al.*, 2012]. Here we use all REMS data products and dust opacities derived from the Mastcam instrument to estimate the SEB and thermal inertia of a few interesting sites along the Curiosity's traverse.

We choose to study sol 82 at RCK, sol 112 at PL, and sol 139 at YKB because these sols are representative of different environmental conditions and soil properties, as what follows from the analysis of ground temperature and UV radiation flux during the first 150 sols shown in Figure 2. From sol 55 to sol 90, the measured UV radiation flux at the surface contains little variability, while the ground temperature increases slowly as the planet approaches its perihelion. Then, around sol 90, a local dust storm causes an abrupt

(hourly) resolutions. Because of this hourly temporal resolution, the depth of the soil sensed by our methodology is the diurnal penetration depth (a few centimeters), thus enabling the calculation of thermal inertia values that do not change with time of day or season if vertical layering is not present in the first few cm.

Curiosity is equipped with a set of analytical and optical instruments [Grotzinger *et al.*, 2012] capable of providing key insights into the SEB and

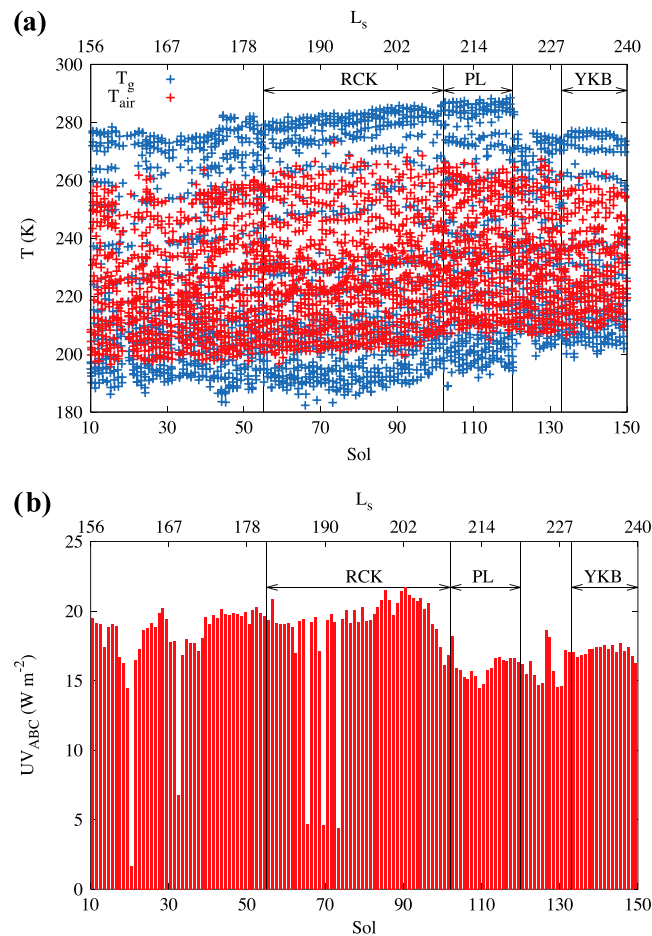


Figure 2. (a) GTS (T_g) and ATS (T_{air}) measurements with the highest confidence level for the first 150 sols. The high confidence level implies the highest quality calibration and no shadows in the field of view. (b) Maximum-measured daily UV radiation fluxes for the same time span. Three time intervals corresponding to the Rocknest (RCK), Point Lake (PL), and Yellowknife Bay (YKB) locations are highlighted in both figures. The environmental conditions and physical soil properties change dramatically between them.

whereas the sources of noninstrumental uncertainty are described in detail by *Hamilton et al.* [2014]. Here we provide an overview of the GTS design and briefly describe the measurement uncertainties.

The REMS GTS is located on the base of a boom about 1.6 m above the ground and facing toward a 120° azimuthal direction (with 0° being the rover forward looking direction, counting clockwise). The sensor is pointed 26° downward from the plane of the rover deck with a field of view of 60° horizontally and 40° vertically. The sensor itself is a set of three thermopiles inside a housing that acts as a thermal mass to reduce temperature gradients in the system. Surface brightness temperatures are derived from the thermopile measurements in the bandwidths 8–14, 15.5–19, and 14.5–15.5 μm, which were chosen to minimize reflected solar irradiance (<0.5%).

Hamilton et al. [2014] report GTS systematic uncertainties of ~2 K just before dawn and ~1 K near midday. Apart from uncertainties associated with the sensor performance, geometric and environmental aspects also influence the accuracy of the GTS measurements. The 60° × 40° FOV covers a ground area of about 100 m², assuming zero roll and pitch angles over flat terrain. This area varies with the rover roll angle and to a lesser extent with pitch angle, both because of the low vertically pointing angle of the GTS. A ±4° roll changes the FOV area from 1331 to 27.9 m². Another geometrical aspect is that the signal per unit area is stronger closer to the rover and on terrain sloped toward it, compared to the farther parts of the FOV and those that slope away

decrease in UV radiation flux from 22 to 15 W m⁻². However, an abrupt decrease in the diurnal amplitude of the ground temperature does not occur until sol 120, with the measured UV radiation showing little variability since sol 90. Thus, the collapse in ground temperature occurring at around sol 120 is not explained by an increase in atmospheric opacity but by a different type of soil.

Figure 3 provides an overview of the three sites analyzed in this article. Each image is a panoramic Navcam mosaic, showing the terrain type around the rover at RCK on sol 82, PL on sol 112, and YKB on sol 139, with the field of view (FOV) of the GTS shaded in green. Additionally, Mastcam color images provide a closer view of the surface of each site. At RCK, sand dominates the near field; most of the GTS signal originates from the sand but the more distant rocky terrain also contributes to the signal. The PL area is also dominated by sandy soil, but in this case the soil is a poorly sorted mix of sand and cobble-sized rock debris. In contrast, sedimentary bedrock dominates the YKB site with fine-grained debris filling narrow domains between bedrocks.

Among all REMS data products used in this article, GTS measurements have the largest impact on the results. The technical description, design, and in-flight calibration of the REMS GTS is described by *Sebastián et al.* [2010],

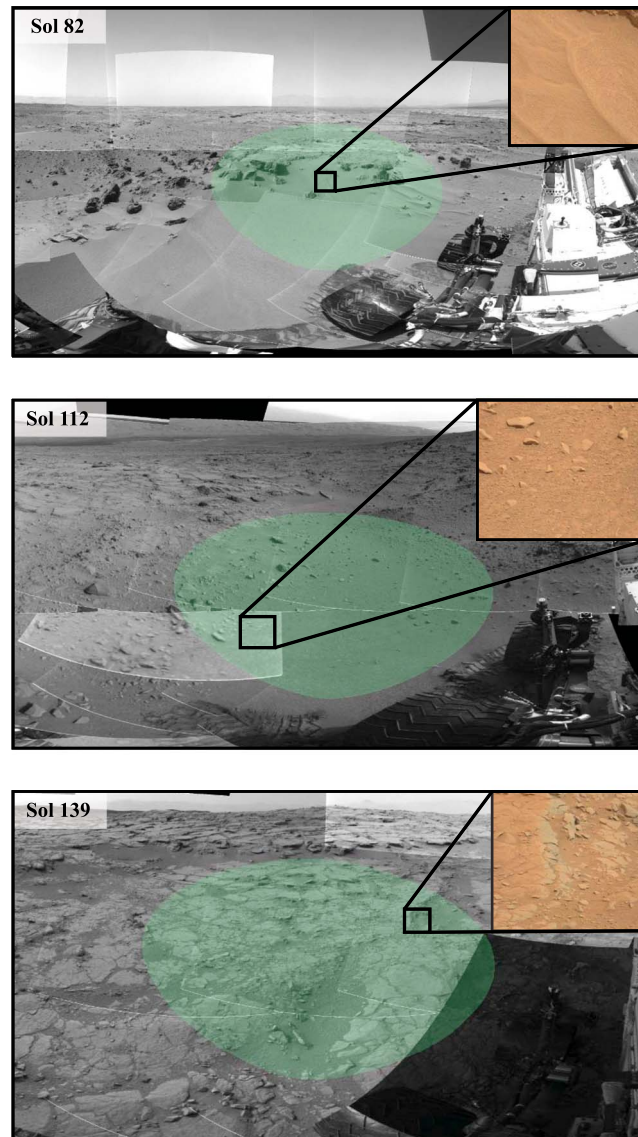


Figure 3. (top to bottom) Rocknest, Point Lake, and Yellowknife Bay Navcam mosaics showing the terrain monitored by the REMS GTS in green for sols 82, 112, and 139, respectively, and higher resolution Mastcam color images from parts of the field of view, providing a closer look at the ground texture representative for each location.

and YKB areas. We study sol 82 at RCK, sol 112 at PL, and sol 139 at YKB. These sols are characteristic of the three periods highlighted in Figure 2 because the hourly average ground temperatures measured during these sols are the closest to the hourly averages over the entire measurement periods at each site. Here hourly average values correspond to averages of the first 5 min of measurements at 1 Hz at each hour during a sol (only values with the highest confidence level are used in the calculations). Figure 4 shows hourly average results of GTS measurements and their standard deviations during these three sols.

UV radiation measurements available in the NASA Planetary Data System (PDS) are used to provide environmental context only, for example, to detect dust storm activity. Dust opacity values in the visible range derived from the Mastcam instrument are used in our calculations (section 3). Air temperature sensor (ATS) data shown in Figure 2 are also used in our calculations. These data are also available in the PDS, but their accuracy is not well understood and they have not been published yet. Here we use ATS data only to calculate the sensible heat flux, which has a modest impact on SEB and on thermal inertia calculations (see section 4).

from the rover. Furthermore, rover shadowing of the GTS FOV reduces the signal by an amount that depends on the physical properties of the soil and the affected portion of the GTS footprint. Another source of uncertainty in the measurements of ground temperature is the rover's radioisotope thermoelectric generator (RTG), which heats the rover and the ground. The temperature of the RTG housing can reach $\sim 200^{\circ}\text{C}$, and even being partially shielded by the heat exchangers, it can increase the apparent ground temperature by up to $\sim 4\text{ K}$. The e -folding radius of influence of the RTG on the surface is about 3.5 m, which overlaps with the near FOV of the GTS responsible for about 50% of the signal. Finally, variations in the emissivity of the ground along the rover's traverse cause uncertainties in the measured brightness temperature. The GTS was calibrated under the assumption of unit surface emissivity, which results in underestimations of the true surface kinetic temperature of a few Kelvins, as described in detail by *Hamilton et al.* [2014].

We use only GTS measurements with the highest confidence level (ASIC power supply in range, highest recalibration quality, and no shadows in the GTS FOV) to maximize the sensor performance. In addition, we use only GTS measurements acquired over moderately flat terrains with the rover still, minimizing the effect of variations in the rover roll angle and variations in the RTG heating. Specifically, we analyze three sols representative of the RCK, PL,

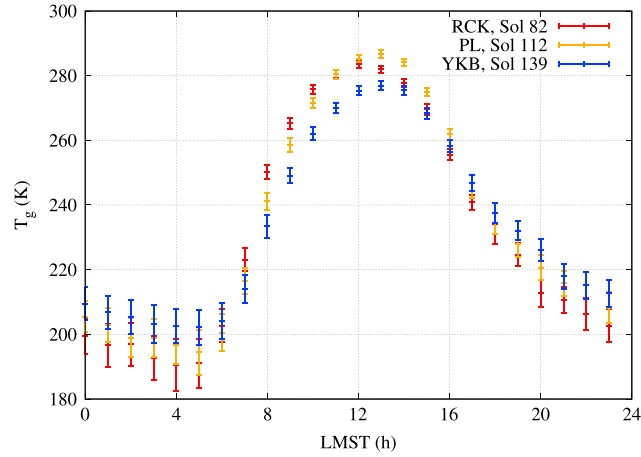


Figure 4. Hourly GTS measurements and their standard deviation for the three sols analyzed in this article: sol 82 at Rocknest (RCK), sol 112 at Point Lake (PL), and sol 139 at Yellowknife Bay (YKB). During these sols, the GTS measurements have high confidence level.

3. Methodology

In this section, we first explain how the various terms involved in the SEB are calculated from REMS measurements and parameters like surface albedo α , surface emissivity ϵ , and dust opacity τ . Due to the uncertainty in these parameters, we consider a range of possible values for each of them and calculate two limiting scenarios for each term of the SEB. In the second part of this section, we develop a new method for calculating the thermal inertia from GTS measurements.

3.1. Derivation of the Surface Energy Budget

The net heat flux into the ground G is used to solve the heat conduction (1-D) equation

$$\rho c_p \frac{\partial T}{\partial t} = \frac{\partial}{\partial z} \left(\lambda \frac{\partial T}{\partial z} \right), \quad (3)$$

applied to the soil by imposing the upper boundary condition

$$-\lambda \frac{\partial T}{\partial z} \Big|_{z=0} = G = Q_{SW}(1 - \alpha) + Q_{LW} - \epsilon \sigma T_g^4 - Q_H - Q_E \quad (4)$$

to it. The calculation of each term of equation (4) is explained next.

3.1.1. Downwelling SW and LW Radiation

We use the radiative transfer model developed by Savijärvi *et al.* [2005] to calculate the downwelling SW and LW radiation fluxes at the surface. The dust opacity in the visible range τ_{VIS} , the column water vapor abundance, and the surface pressure are used to calculate Q_{SW} and Q_{LW} . The model allows for potential formation of clouds, fog, and ground frost. In situ measurements by Viking, Pathfinder, the Mars Exploration Rovers, and the Phoenix lander have been simulated successfully using this model [Martínez *et al.*, 2009; Savijärvi and Määttänen, 2010].

Values for τ_{VIS} are taken from Mastcam observations (M. Lemmon, personal communication, 2013). Around sol 82, τ_{VIS} was within the range 0.55–0.65, while on sols 112 and 139 τ_{VIS} was within the range 0.9–1. Values for the albedo are taken from satellite estimations by TES at Gale Crater and are within the range 0.20–0.25 [Pelkey and Jakosky, 2002]. Finally, surface pressure is provided by REMS, while column water vapor abundances are taken from TES estimations, with typical low-latitude values of 10 pr μm [Smith, 2004].

In order to calculate a range of possible values for Q_{SW} and Q_{LW} , we use extreme values of α and τ_{VIS} . Specifically, $Q_{SW}(1 - \alpha)$ is maximum (minimum) when both α and τ are minimum (maximum), whereas Q_{LW} is maximum (minimum) when τ is maximum (minimum).

3.1.2. Upwelling LW Radiation

Upwelling LW radiation is calculated from the expression $\epsilon \sigma T_g^4$, with ϵ in the range 0.9 to 1, as derived from laboratory experiments with Mars analogues and the Mini-TES instrument aboard the MERs rovers [Christensen *et al.*, 2004a]. Here ϵ values represent spectral averages in the thermal infrared domain.

Similarly to the downwelling SW and LW radiation, we calculate a range of possible values for $\epsilon \sigma T_g^4$ by using extreme values of ϵ and T_g . This term is maximum when both ϵ and T_g are maximum. The maximum in T_g refers to its mean values plus the standard deviation shown in Figure 4, while the minimum in T_g refers to its mean values minus the standard deviation.

3.1.3. Sensible Heat Flux

The sensible heat flux is calculated using the expression

$$Q_H = k^2 c_p u \rho_a f(R_B) \frac{(T_g - T_a)}{\ln^2(z_a/z_0)}, \quad (5)$$

where $k = 0.4$ is the von Karman constant, $c_p = 736 \text{ J Kg}^{-1} \text{ K}^{-1}$ is the specific heat of CO_2 at constant pressure, $\rho_a = P/RT_a$ is the density of the air at 1.6 m, P is the surface pressure, $R = 189 \text{ J Kg}^{-1} \text{ K}^{-1}$ is the gas constant of the Martian air, $z_a = 1.6 \text{ m}$ is the height at which the air temperature T_a and horizontal wind speed u are measured, z_0 is the surface roughness, and $f(R_B)$ is a function of the bulk Richardson number R_B that accounts for the thermal stability in the near surface. Equation (5) follows the drag transfer method applied to Mars with the peculiarity that $f(R_B)$ has been tested successfully under Earth Polar conditions and therefore is suitable for applications at cold dry Martian-like conditions [Savijärvi and Määttänen, 2010].

Except for z_0 , all the parameters in equation (5) are either known or measured by REMS (R_B can be calculated from T_g , T_a , and u). Based on TES measurements at Gale Crater, we assume values for surface roughness ranging from 0.5 to 1.5 cm [Hébrard et al., 2012]. These values must be used cautiously because of their low spatial resolution ($1/8^\circ \times 1/8^\circ$). Fortunately, the impact of the sensible heat flux on the net heat flux is only modest, as it will be shown in the next section.

Maximum and minimum values of Q_H are obtained when the absolute value of the difference ($T_g - T_a$), z_0 and u are maximum and minimum, respectively. We point out that REMS wind speed data are not yet available on NASA's Planetary Data System. Here we use data based on preliminary calibrations indicating typical maximum values of about 10 m s^{-1} and minimum values of about 4 m s^{-1} .

3.1.4. Latent Heat Flux

The latent heat flux is calculated using the expression

$$Q_H = L_v \beta k^2 c_p u \rho_a f(R_B) \frac{[q_s(T = T_g) - q_a]}{\ln^2(z_a/z_0)}, \quad (6)$$

where $L_v = 2.83 \times 10^6 \text{ J kg}^{-1}$ is the latent heat of sublimation for water vapor, β is the top soil moisture availability, q_s is the saturation specific humidity at $T = T_g$, and q_a is the specific humidity at z_a .

This term can be neglected in the SEB because it is of the order of 1 W m^{-2} at most. This is proven by performing a scale analysis on equation (6) with typical values for $\rho_a \sim 10^{-2} \text{ kg m}^{-3}$, $q_a \sim 10^{-4} \text{ kg kg}^{-1}$, $u \sim 10 \text{ m s}^{-1}$, $q_s(T = T_g)$ in the range 10^{-5} to $10^{-1} \text{ kg kg}^{-1}$ (these values being consistent with REMS data), β equal to 1 in case of frost formation (not detected by MSL yet) and $\sim 10^{-4}$ otherwise (in order to keep the precipitable water content around 5 pr μm) [Savijärvi, 1999; Smith et al., 2006], $f(R_B)$ between 0 and 1, and $1/\ln^2(z_a/z_0) \sim 10^{-2}$.

3.2. Derivation of Thermal Inertia

The thermal inertia is calculated by solving the heat conduction equation applied to the soil. Using the definition of I described by equation (2), equation (3) can be rewritten as

$$\frac{\partial T}{\partial t} = \left(\frac{I}{\rho c_p} \right)^2 \frac{\partial^2 T(z, t)}{\partial z^2}, \quad (7)$$

where λ is assumed to be constant with depth. Instead of using the upper boundary condition described by equation (4), we now solve equation (7) by imposing the alternative upper boundary condition

$$T(0, t) = T_g(t) \quad (8)$$

where $T_g(t)$ stands for REMS GTS measurements. The second boundary condition required to solve equation (7) is the lower boundary condition

$$T(z_d, t) = T_d, \quad (9)$$

where z_d is the depth at which the subsurface temperature is constant and equal to T_d .

The solution to equation (7) is the vertical profile of the subsurface temperature $T(z,t)$, from which the net heat flux into the ground G can be obtained from the equation

$$G = -\lambda \left. \frac{\partial T(z,t)}{\partial z} \right|_{z=0} \approx \frac{l^2}{\rho c_p} \frac{T(\delta,t) - T(0,t)}{\delta}, \quad (10)$$

where δ is the depth of the topmost soil layer of our numerical model.

We define G^* as the net surface forcing obtained from the right side of equation (10) to differentiate it from G obtained using the SEB as described in equation (4). Although both G^* and G represent the net heat flux into the ground, they are obtained by different methods and depend on different parameters. Whereas G^* is calculated using equations (7)–(10) and depends on l , z_d , T_d , and ρc_p , G is calculated using equation (4) and the procedure described in the previous subsection.

In the new method proposed in this article, the thermal inertia of the soil is determined by calculating the value of l that provides the best match between G^* and G . We show in section 4.2 that this approach is possible because for reasonable values of z_d , T_d , ρc_p , and l , the function $G^*(z_d, T_d, \rho c_p, l)$ is reduced to the function $G^*(l)$.

3.2.1. Comparison to Other Approaches

Values of thermal inertia of the Martian soil have generally been calculated using satellite measurements. Typical THEMIS and TES spatial resolutions range from 10^4 to 10^7 m², with temporal resolutions of single-point measurements per day. Due to their large spatial and temporal resolution, surface temperature measurements by satellite are affected by surface heterogeneities, which range horizontally within the sensor footprint and vertically from a few decimeters to a few meters of depth [Putzig and Mellon, 2007]. Therefore, thermal inertias estimated from orbit show an apparent change when a homogeneous model is used where layering is present (when an appropriate model is used, both layering and thermal inertia are properly derived).

In this study, we use GTS measurements at high spatial ($\sim 10^2$ m²) and temporal (hourly) resolutions to complement satellite estimations of surface thermophysical properties at Gale Crater [Pelkey and Jakosky, 2002; Christensen et al., 2001; Putzig et al., 2005; Putzig and Mellon, 2007; Fergason et al., 2012]. Since we calculate the thermal inertia by solving the heat conduction equation using GTS measurements provided in a subdiurnal scale in equation (8), the depth of the soil sensed by our methodology corresponds to the diurnal penetration depth (a few centimeters). This enables the calculation of thermal inertia values that do not change with time of day or season if vertical layering is not present in the top few centimeters.

Our results also complement thermal inertia calculations at Gale Crater carried out by Hamilton et al. [2014]. Although GTS measurements are used in both studies, the methods used to calculate l are quite different. While Hamilton et al. [2014] use GTS measurements only as a reference to determine the value of l that produces the best match between the output of a thermal model [Kieffer, 2013] and GTS measurements, we use GTS measurements as an input (see equation (8)) to solve the heat conduction equation (equation (7)) and thus determine l , as explained in the previous section. We show in section 4 that both procedures yield similar results.

4. Results

In this section, we first calculate the values of the various terms of the SEB shown in equation (4). Then, we determine l by solving the heat conduction equation in the soil shown in equation (7) using equations (8) and (9) as boundary conditions.

4.1. Surface Energy Budget Values

Following the sign convention used in equation (1), downward fluxes are defined as positive (heating), whereas upward fluxes are defined as negative (cooling). Notice though that the sensible heat flux Q_H is preceded by a minus sign in equation (1). Thus, negative values of Q_H imply surface heating whereas positive values imply surface cooling.

Figure 5 and Table 1 show values of the various terms of the SEB derived using equation (4) applied to data obtained at RCK, PL, and YKB. At each site, the net heat flux into the ground G during the daytime is positive

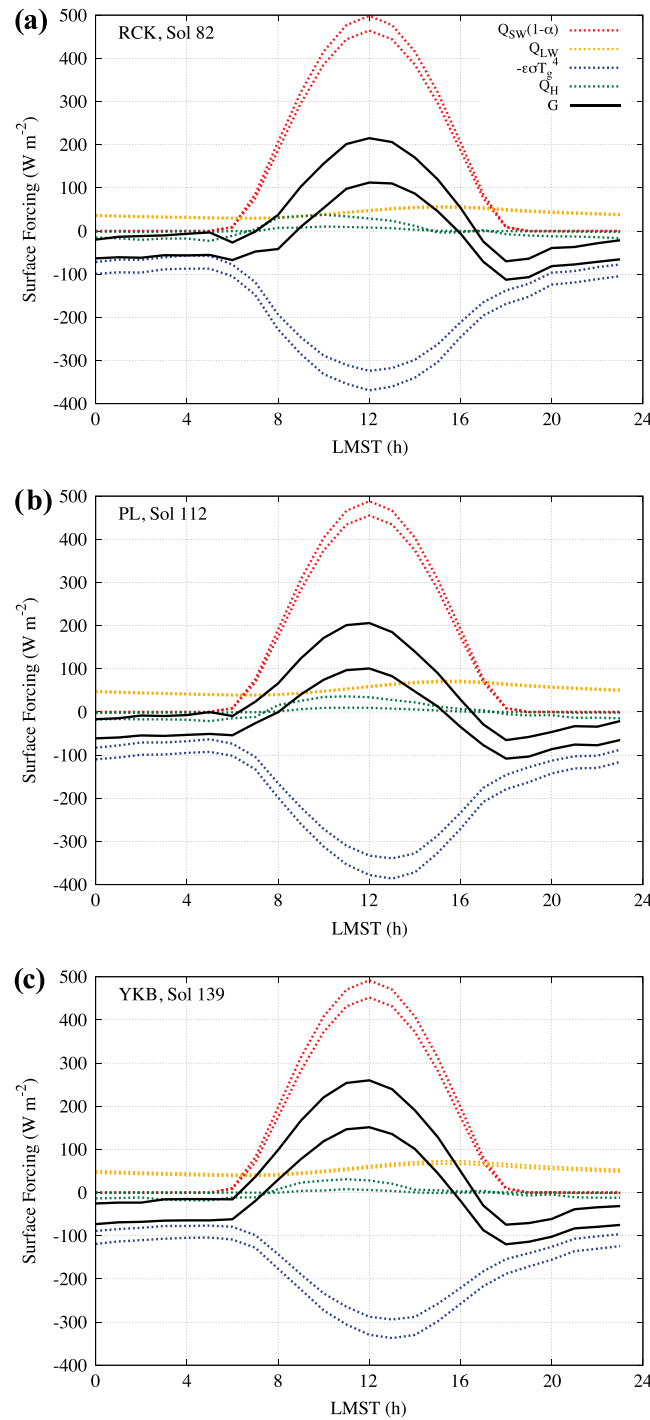


Figure 5. The various terms of the surface energy budget at (a) Rocknest (RCK), (b) Point Lake (PL), and (c) Yellowknife Bay (YKB) showing the maximum and minimum values obtained for shortwave radiation $Q_{SW}(1 - \alpha)$, upwelling and downwelling longwave radiation $\epsilon\sigma T_g^4$ and Q_{LW} , sensible heat flux Q_H , and the resulting net surface forcing G for the three sols.

values as low as -18 W/m^2 through meteorological modeling for the nighttime sensible heat flux under similar wind speeds, although over steeper terrains than those analyzed here.

The downwelling LW radiation flux from the atmosphere presents the lowest diurnal variability among the terms shown in Figure 5. It peaks between 1500 and 1600 LMST at each site, which is consistent with the time

and it is overwhelmingly dominated by two terms: the downwelling SW radiation flux ($\sim 400\text{--}500 \text{ W/m}^2$) and the surface upwelling LW radiation flux ($\sim 300\text{--}400 \text{ W/m}^2$). Together, they account for at least 70% of G between 0900 and 1400 local mean solar time (LMST). Downwelling LW radiation flux and sensible heat flux are 1 order of magnitude smaller than the dominant terms (see Figure 5), thus playing minor roles in the SEB. The former heats the surface, whereas the latter removes heat from it [Martínez et al., 2011]. The moderate atmospheric dust content ($\tau < 1$) and the low atmospheric density ($\sim 10^{-2} \text{ kg m}^{-3}$) explain the low values for these two terms. At night, the net surface forcing is negative and is dominated by the surface upwelling LW radiation flux ($\sim 60\text{--}100 \text{ W/m}^2$) and the downwelling LW radiation flux from the atmosphere ($\sim 50 \text{ W/m}^2$). Since near-surface temperature inversions occur every night, the nighttime sensible heat flux is directed toward the surface, thus warming it up. Under high wind conditions ($u \sim 10 \text{ m/s}$), the turbulent heat flux can take negative values down to -20 W/m^2 , thus playing a secondary but not negligible role in the SEB. Previous nighttime estimations of sensible heat flux derived from numerical models at Viking, Pathfinder, and Phoenix landing sites suggest minimum values of about -5 W m^{-2} [Haberle et al., 1993; Martínez et al., 2009; Savijärvi and Määttänen, 2010]. Even though we use similar drag transfer methods and Richardson number formulations as those used in previous studies, we obtain values of sensible heat fluxes of up to 4 times larger (see Table 1). Our high values correspond to the limiting scenario for Q_H that results from the use of extreme (but attainable) values of ground and air temperature, horizontal wind speed, and surface roughness (see section 3). More recently, Spiga et al. [2011] obtained

Table 1. Maximum and Minimum Values for the Various Terms of the SEB^a

	RCK, Sol 82			PL, Sol 112			YKB, Sol 139		
	Max (W/m ²)	Min (W/m ²)	LT (h)	Max (W/m ²)	Min (W/m ²)	LT (h)	Max (W/m ²)	Min (W/m ²)	LT (h)
$Q_{SW}(1 - \alpha)$	498	0	12/18–6	488	0	12/18–6	492	0	12/18–6
Q_{LW}	57	28	15/7	72	38	16/7	73	38	15/7
$\varepsilon\sigma T_g^4$	369	57	12/4	386	63	13/5	337	76	13/5
Q_H	38	–23	10/5	36	–21	11/5	31	–18	11/5
G	215	–113	12/18	206	–108	12/18	260	–120	12/18
ΔT_g		93.0			92.2			74.8	

^aThese terms have been derived from extreme but possible values of albedo (α), surface emissivity (ε), dust opacity (τ), and GTS measurements. In this study, α is assumed to be in the range 0.20 to 0.25 and ε in the range 0.9 to 1. However, τ takes different values due to a local dust storm initiated between sol 82 and sol 112. Thus, τ is between 0.55 and 0.65 at RCK, whereas at PL and YKB it is between 0.9 and 1. LT stands for local time.

at which REMS air temperatures peak. Previous estimations of this term calculated by *Määttänen and Savijärvi* [2004] at the Pathfinder landing site and by *Savijärvi* [1995] at the Viking landing site show maxima between 1500 and 1600 LMST as well, although the values shown there are smaller than in Figure 5 due to the lower atmospheric opacity at the times those landing sites were observed.

We show in Figure 5 the uncertainty in the net heat flux into the ground, which is represented by the area enclosed by solid black lines. We obtain this uncertainty by adding the different terms of the SEB shown in Figure 5. The ranges of potential values considered for the albedo, surface emissivity, dust opacity, and ground temperature, which were described in section 3, account for the uncertainty in each individual term. Quantification of these errors is used to calculate the relative error in thermal inertia and is presented in section 5.

4.2. Calculations of the Thermal Inertia

Before calculating the thermal inertia, we study the sensitivity of the net heat flux into the ground G^* obtained using equations (7)–(10). We show that for reasonable values of ρc_p , z_d and T_d , $G^*(z_d, T_d, \rho c_p, l)$ reduces to $G^*(l)$. Then, we calculate the thermal inertia by determining the value of l that provides the best match between G^* and G .

4.2.1. Sensitivity Studies

In order to solve equations (7)–(10), typical values for ρc_p , z_d , T_d , and l need to be known. We show typical values of each of these quantities next. A moderate range of values for the volumetric heat capacity of the Martian soil (ρc_p) is found in the literature. *Möhlmann* [2004] suggests a value of $1.255 \times 10^6 \text{ J m}^{-3} \text{ K}^{-1}$, similar to that for basaltic material. For basaltic material at Gale Crater, *Blake et al.* [2013] use a soil density of $\rho = 3000 \text{ Kg m}^{-3}$. Assuming typical values of $c_p = 560 \text{ J Kg}^{-1} \text{ K}^{-1}$ for basaltic soils at temperatures around 200 K, $\rho c_p = 1.7 \times 10^6 \text{ J m}^{-3} \text{ K}^{-1}$ is obtained. Finally, *Edgett and Christensen* [1991] use values between 0.8 and $1.3 \times 10^6 \text{ J m}^{-3} \text{ K}^{-1}$ for Martian aeolian dunes, while *Savijärvi* [1999] assumes values of $0.8 \times 10^6 \text{ J m}^{-3} \text{ K}^{-1}$ for dry sandy soil. We conclude that values between 0.8 and $1.7 \times 10^6 \text{ J m}^{-3} \text{ K}^{-1}$ are a reasonable approximation for the volumetric heat capacity of the Martian soil.

Since we solve the heat conduction equation during single diurnal cycles, the depth z_d at which the subsurface temperature can be considered to be invariant is about 2–3 times larger than the diurnal e-folding or penetration depth $L = \sqrt{(2/\omega)(l/\rho c_p)}$, where $\omega = 7.0774 \times 10^{-5} \text{ s}^{-1}$ is the angular speed of the planet's rotation. Considering the values for ρc_p described above, and typical values of l of the order of a few hundred SI units, the diurnal penetration depth is a few centimeters. Therefore, we can safely assume that $z_d \sim 10 \text{ cm}$.

Finally, reasonable values for T_d can be obtained using the data shown in Figure 4 and physical considerations. We assume values of T_d in the range 200–230 K. The lower 200 K bound is taken because in order to ensure a restoring (upward) heat flux from the deep soil (depths $> z_d$), T_d must be higher than the minimum daily ground temperature (184 K at RCK 82, 191 K at PL 112, and 198 K at YKB 139, as shown in Figure 4). In addition, the higher 230 K bound is taken because T_d values slightly below the daily average ground temperature ($\sim 234 \text{ K}$ at RCK 82, $\sim 239 \text{ K}$ at PL 112, and $\sim 237 \text{ K}$ at YKB) provide the most accurate solution to the heat conduction equation at diurnal scales [*Savijärvi*, 1995; *Savijärvi and Määttänen*, 2010]. As explained next, the uncertainty in G^* caused by changes of T_d within the assumed range is modest.

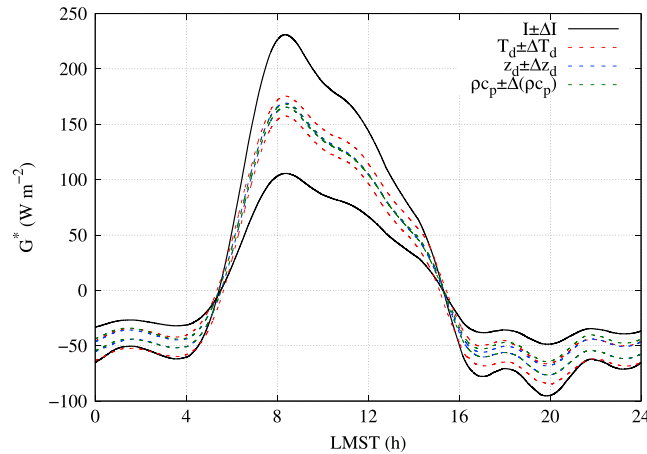


Figure 6. Sensitivity of G^* on sol 82 at Rocknest. Here ρc_p is varied between 0.8 and $1.6 \times 10^6 \text{ J m}^{-3} \text{ K}^{-1}$, z_d between 7 and 13 cm, T_d between 200 and 230 K, and thermal inertia between 175 and 375. The heat flux into the ground (calculated from solving the heat conduction equation in the soil using REMS GTS measurements as an upper boundary condition) depends mostly on thermal inertia. Similar results are obtained at Point Lake and Yellowknife Bay.

Figure 6 shows that the net heat flux into the ground, derived from equations (7)–(10), depends mainly on the thermal inertia. Throughout the day, the greatest variation in G^* , represented by the area between the black solid lines in Figure 6, is caused by variations in the values assumed for the thermal inertia. In particular, G^* varies by up to 40% with variations in thermal inertia (ΔI) during the daytime, followed by a smaller variation of 5%, 1.5%, and 1% caused by ΔT_d , $\Delta(\rho c_p)$, and Δz_d , respectively. At night, G^* is more sensitive to T_d , ρc_p , and z_d than during the day. In this case, G^* varies up to 33% with ΔI , followed by a variation of 20%, 15%, and 10% introduced by ΔT_d , $\Delta(\rho c_p)$, and Δz_d .

It is important to point out that regardless of the values imposed on ρc_p , z_d , T_d , and I , any diurnal evolution of G^*

derived using equations (7)–(10), and then used as an upper boundary condition, as in equation (4), to solve the heat conduction equation, can simulate REMS GTS measurements with an accuracy better than 0.2 K. This is shown for YKB in Figure 7, while similar results are obtained for RCK and PL. Consequently, there are multiple values of I (and also of T_d , ρc_p , and z_d , although these have a lower impact) that produce a perfect match to REMS GTS measurements. Thus, an independent condition must be imposed on G^* to determine which value of the thermal inertia is the most reasonable physically. This condition is explained below.

4.2.2. Thermal Inertia Values

We determine the most physically reasonable value of the thermal inertia by minimizing the function

$$C(I) = \Delta G^*(I) - \Delta G, \quad (11)$$

where $\Delta G^*(I)$ is the amplitude of the diurnal cycle of the net surface forcing calculated from equations (7) to (10)

and ΔG is the diurnal amplitude of the net surface forcing obtained from equation (4) and shown in Figure 5. We use equation (11) to calculate I because, as shown in Figure 6, (i) the thermal inertia regulates the amplitude of G^* but does not change the time at which it peaks, and (ii) regardless of the value of I , T_d , ρc_p , and z_d , the net surface forcing values of G^* and G do not necessarily peak at the same time. Thus, attempts to minimize the function

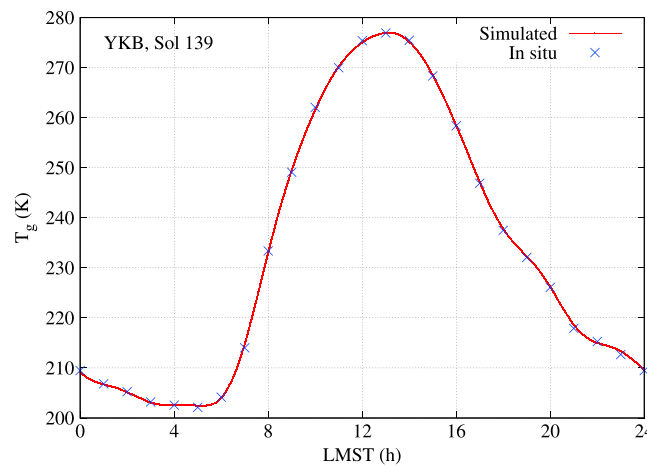


Figure 7. There are multiple values of thermal inertia that can perfectly simulate REMS GTS measurements. Here we show values of I ranging from 175 to 375, all of which provide the right solution to the heat conduction equation in the soil (red curve), almost independently from T_d , ρc_p , and z_d , as shown in Figure 6. Therefore, an additional condition is needed to determine I .

yield unrealistic results for the thermal inertia. For instance, G^* peaks at around 0830 LMST at RCK during sol 82 (see Figure 6), whereas G peaks at noon (see Figure 5a). A similar temporal shift in the peak of G^* and G is found at PL and YKB.

$$C_{\text{alt}}(I) = \frac{1}{N} \sum_{j=1}^N [G^*(t_j) - G(t_j)]^2 \quad (12)$$

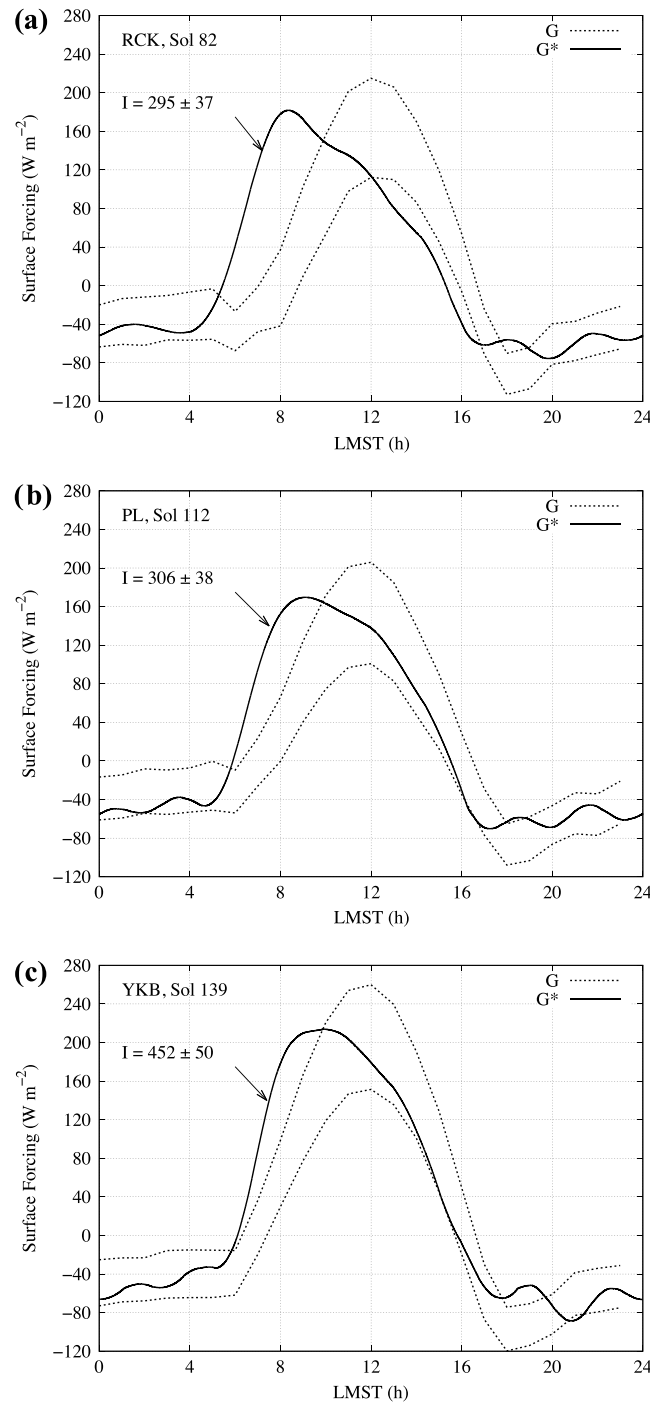


Figure 8. Thermal inertia values (I) at (a) Rocknest (RCK), (b) Point Lake (PL), and (c) Yellowknife Bay (YKB) derived from equation (11). The solid lines represent the net surface forcing derived solely from REMS GTS measurements, whereas the dashed lines represent the net surface forcing derived from all terms involved in the surface energy budget, as shown in Figure 5.

evolution of G and G^* are at least partially explained by spurious or real heating of the surface or the GTS not accounted for in equation (4). A detailed analysis of the departures between G^* and G and possible explanation for them are given in section 5.

Figure 8 shows the values of the thermal inertia at RCK, PL, and YKB obtained using equation (11). The solid line represents the net surface forcing G^* derived only from REMS GTS measurements via equations (7)–(10), whereas dashed lines represent the net surface forcing G derived from equation (4) and shown in Figure 5. The values for z_d , T_d , and ρc_p used to calculate G^* are $T_d = 215$ K, $z_d = 10$ cm, and $\rho c_p = 1.0 \times 10^6$ J m⁻³ K⁻¹ at RCK, $T_d = 215$ K, $z_d = 10$ cm, and $\rho c_p = 1.25 \times 10^6$ J m⁻³ K⁻¹ at PL, and $T_d = 210$ K, $z_d = 12.5$ cm, and $\rho c_p = 1.5 \times 10^6$ J m⁻³ K⁻¹ at YKB. Variations of these parameters within reasonable ranges have a negligible impact on G^* , as shown in the previous subsection.

YKB has the largest value of thermal inertia, $I = 452$ J m⁻² K⁻¹ s^{-1/2} (SI units used throughout this article), followed by PL with $I = 306$ and RCK with $I = 295$ (see Figure 8). These values are consistent with the type of terrain revealed by Mastcam images. Fine-grained and loosely packed material, such as that at RCK, typically exhibits low values of thermal inertia, whereas higher values are common for rocks and exposed bedrock, as at YKB.

The values of the thermal inertia shown in Figure 8 are also consistent with previous estimations at Gale Crater. Using thermal modeling to fit it to GTS measurements, *Hamilton et al.* [2014] reported a most likely value of 300 SI units for RCK. Using predawn TES data, *Christensen et al.* [2001] and *Putzig et al.* [2005] estimated thermal inertias for Gale Crater ranging from 335 to 425 SI units, while *Putzig and Mellon* [2007] estimated lowest values of 287 SI units from daytime values. Also for Gale Crater, but using THEMIS data, *Ferguson et al.* [2012] estimated thermal inertia values of 365 ± 50 SI units at the landing ellipse. Thus, our results are in excellent agreement with previous values obtained by different methods.

Discrepancies between the temporal

The calculations of I at each location have an overall relative error of $\sim 12\%$. This error is caused mostly by uncertainties in the diurnal amplitude ΔG described by equation (11), which corresponds to the area enclosed between the solid black lines in Figure 5. In the next section, we quantify the impact of the uncertainties in the albedo, surface emissivity, ground temperature, and dust opacity on the calculations of thermal inertia.

5. Discussion

Here we first discuss the mechanisms that might explain the differences between the net surface forcing shown in Figure 8. Then we analyze the uncertainty in the calculation of thermal inertia. Finally, we discuss how measurements of thermal inertia along the traverse of a rover support geologic mapping and scientific interpretation.

5.1. Net Surface Forcing Considerations

The net surface forcing G obtained using equation (4) and the quantity G^* obtained using equations (7)–(10) are shown in Figure 8. Three main characteristics of each of the three sites studied are highlighted next. First, G^* increases at a much faster rate than G between 0600 and 0900 LMST. Second, G peaks at 1200 LMST at RCK, PL, and YKB, whereas G^* peaks at around 0830 LMST at RCK and around 0900 LMST at PL and YKB. Third, G^* decreases at a slower rate than G from 1000 to 1700 LMST. Typically, numerical models calculate the ground temperature by solving equation (7), using the ideal net heat flux (G) shown in equation (4) as an upper boundary condition [Kieffer, 2013; Savijärvi and Mänttinen, 2010]. Therefore, if the net heat flux G^* obtained by solving equation (7) using GTS measurements is different from G , it implies that modeled and ground-based surface temperature values differ from each other. This is consistent with previous results, as shown in Hamilton *et al.* [2014, Figure 11]. There, model-predicted temperatures rise later in the morning, peak later, and cool earlier in the afternoon, which follows from the behavior of G and G^* shown in Figure 8. Specifically, the largest difference between modeled ground temperature and GTS measurements at RCK occurs between 0800 and 0900 LMST, with model temperatures underestimated by 15 to 20 K. This coincides with the peak in G^* at RCK shown in Figure 8 of this article.

In order to understand the departures between G and G^* shown in Figure 8 we analyze possible explanations for them. One possible explanation is the use of incorrect values for the various physical parameters used to calculate G and G^* . We studied the sensitivity of the peak in G to α , ε , and τ and in G^* to z_d , T_d , ρc_p , and I . Our studies indicate that neither the peak in G^* nor the peak in G could be shifted enough for agreement between G and G^* . On one hand, G^* peaks at each location between 0830 and 0900 LMST regardless of any reasonable values for z_d , T_d , ρc_p , and I (see Figure 7). On the other hand, G peaks at 1200 LMST regardless of any reasonable values for α , ε , and τ . We also used possible combinations of the values of these parameters beyond the reasonable range described in section 3 but still were not able to find agreements.

The assumption of vertical homogeneity used in the derivation of equation (7) could also explain differences between G and G^* . However, the depth of the soil sensed by our methodology is of the order of a few centimeters (diurnal penetration depth), and it is unlikely that this assumption would lead to similar differences in the various locations. In addition, vertical layering cannot explain the fact that G^* decreases at a slower rate than G in the afternoon. This is because such a differential rate of decrease implies model surface temperatures colder than GTS measurements, and when a two-layer subsurface model is used, the problem of overly warm measured surface in the afternoon remains [Hamilton *et al.*, 2014].

Discrepancies between G and G^* could also be explained by heating mechanisms not accounted for in equation (4) but reflected in the GTS measurements. Heating of the surface by the RTG and its heat exchangers is not accounted for in equation (4). The e -folding radius of influence of the RTG on the surface is about 3.5 m, which overlaps with the near FOV of the GTS from which 50% of the signal comes. Nonetheless, just irradiation of the surface by the RTG is unlikely to explain the offset between G and G^* . Since the departures between G and G^* shown in Figure 8 are recurrent during the first 150 sols, mechanisms to explain them must also be recurrent. Since rover activities and thus the temperature of the heat exchangers irradiating the GTS FOV varied from sol to sol, we believe that it is unlikely that the radiation from the RTG and surrounding heat exchangers can cause the recurrent impact on GTS measurements.

Table 2. Analysis of the Uncertainty in the Thermal Inertia as a Function of the Various Parameters Used in Its Calculation

	$\Delta\alpha = 0.025$	$\Delta\varepsilon = 0.05$	$\Delta T_g = 1-5 \text{ K}$	$\Delta\tau = 0.05$
$\Delta I/I = 12.5\%$	5%	3.5%	3.3%	0.7%

A potential explanation for discrepancies between G and G^* is the possible degradation of the GTS during the trip to Mars, which could reduce the sensitivity of the sensor. The loss of sensitivity may explain why the largest discrepancies between G and G^* occur between 0600 and 0900 LMST (Figure 8), which corresponds to the times of day when rate of temperature change is the largest (Figure 7). This possible degradation of the GTS sensor is not a well understood process, and thus, its impact on the net heat flux cannot be quantified yet. Nonetheless, this appears to be the most likely explanation for the differences between G and G^* .

5.2. Error Analysis of Thermal Inertia Calculations

We calculate the thermal inertia with an overall error of $\sim 12\%$ (see Figure 8), which is caused mainly by uncertainties in the range of values considered for the albedo, surface emissivity, ground temperature, and dust opacity. First, we quantify the impact of the uncertainties in these parameters on the diurnal amplitude of the net surface forcing ΔG (area enclosed by the solid black lines in Figure 5). During the day, the largest sources of error are the uncertainties in the albedo and the surface emissivity, followed by the ground temperature, and then the dust opacity. At night, uncertainties in ground temperature are responsible for the largest source of error, followed by the surface emissivity and the dust opacity. Second, we quantify the impact of ΔG on thermal inertia calculations via equation (11). Finally, we use these results to calculate the overall uncertainty in I . The results of these calculations are summarized in Table 2 and discussed below.

The uncertainty in the albedo $\Delta\alpha = 0.025$ is responsible for the largest source of error, with a relative contribution of 5%. The albedo affects the largest term in the SEB (see Figure 5), and thus, small variations in albedo affect the net surface forcing significantly and therefore impact the determination of the value of the thermal inertia. Uncertainties in surface emissivity $\Delta\varepsilon = 0.05$ and ground temperature $\Delta T_g = 1 - 5 \text{ K}$ have a similar impact on the thermal inertia, both contributing 3.5% toward the overall uncertainty of 12%. Finally, the uncertainty in the dust opacity $\Delta\tau = 0.05$ barely affects the determination of the value of the thermal inertia. The reason for this is that for moderate values of the dust opacity (as was the case for the sols analyzed here), the downwelling LW radiation at the surface is 1 order of magnitude lower than the dominant terms of the SEB.

Using THEMIS data, *Ferguson et al.* [2012] calculate I with a relative error of $\sim 20\%$, with the largest source of error being uncertainties in the instrument calibration, followed by uncertainties in albedo, atmospheric opacity, and surface temperature values, which were retrieved with an uncertainty below 2.8 K. Using TES data, *Mellon et al.* [2000] calculate thermal inertia with a relative error of 6% for surface temperature of 180 K. In this case, an uncertainty in albedo of $\Delta\alpha = 0.1$ is assumed. Our method results in intermediate errors ($\sim 12\%$), but more importantly, the surface measurements by Curiosity allow the calculation of thermal inertia at much higher spatial resolution.

5.3. Evaluation of Local Geology From High-Resolution Ground-Based Measurements

Estimations of I along the rover traverse support geologic mapping and data interpretation when used simultaneously with images and other data sets. In particular, we show that the joint assessment of the SEB and thermal inertia values provides an excellent context for evaluating the local geology. For instance, we show that although dust opacity values (and thus the radiative forcing) are very similar at PL and YKB (Table 2), soil thermal inertia values are dramatically different (~ 306 versus ~ 452). Thus, measurements of thermal inertia unveil horizontal surface heterogeneities below $\sim 50 \text{ m}$ (distance between both locations, Figure 1). This provides context for Mastcam color images capturing the texture of the surface (Figure 3).

Studies of thermal inertia from ground-based measurements are important because the lack of information about the shallow subsurface is a significant challenge to rovers. A rover traversing nearly horizontal sedimentary rocks would have limited knowledge of the subsurface. Variations in thermal inertia could be correlated with local outcrops and traced laterally, providing a broader knowledge of the local geology than provided by cameras and contact instruments.

Martian sedimentary rocks often exhibit sedimentary structures indicative of the environment at the time of their deposition. These have been observed and interpreted using surface and contact measurements [Squyres *et al.*, 2004; Grotzinger *et al.*, 2013]. The Opportunity, Spirit, and Curiosity rovers have shown that shallow bedrock is usually covered by loose material, such as dust, sand, or regolith. While images can be used to delineate areas of exposed bedrock and surficial materials, they do not unveil the shallow subsurface. Indeed, the presence of sedimentary structures below a thin layer of regolith is not easily detectable. Measurements of thermal inertia are capable of unveiling these structures when they are present in the shallow subsurface. Thus, measurements of thermal inertia along a rover traverse provides complementary information about the shallow subsurface not revealed by typical measurements.

6. Summary and Conclusions

Ground-based estimates of thermal inertia augment surface observations, providing context for evaluating the local geology. Here we use GTS measurements to determine the thermal inertia at a few locations in Gale Crater at a horizontal resolution of $\sim 10^2$ m² and a vertical resolution of a few centimeters. Our results complement satellite measurements at Gale Crater at horizontal resolutions ranging from $\sim 10^4$ to $\sim 10^7$ m² and vertical resolutions ranging from a few decimeters to a few meters, thus enabling the calculation of thermal inertia values that do not change with time of day or season if vertical layering is not present in the first few centimeters.

We calculate the thermal inertia by solving the heat conduction equation in the soil with in situ hourly averaged measurements of the ground temperature as an upper boundary condition. We only use measurements of the highest confidence level. The largest value of the thermal inertia $I = 452 \pm 50$ was found at YKB, followed by PL with $I = 306 \pm 38$ and RCK with $I = 295 \pm 37$. These values are in excellent agreement with previous TES and THEMIS satellite estimations at Gale Crater (see section 4.2.2) and with thermal inertia values derived by Hamilton *et al.* [2014] using thermal modeling to fit it to GTS measurements. Finally, the values of thermal inertia that we obtain are also consistent with the type of terrain imaged by Mastcam (Figure 4). Fine-grained and loosely packed material such as that found at RCK typically has low thermal inertia values, whereas higher values are common for rocks and exposed bedrock, as in YKB.

Additionally, we report analysis of the SEB in Gale Crater by using ground-based measurements taken by the Curiosity rover. We have reported values of thermal inertia and SEB during three sols representative of different environmental conditions and soil properties, sol 82 at RCK, sol 112 at PL, and sol 139 at YKB. The results shown in this paper are essentially identical to those for other sols corresponding to the same periods and same terrain.

At each site analyzed here, the downwelling SW solar radiation flux (~ 400 – 500 W/m²) and the surface upwelling LW radiation flux (~ 300 – 400 W/m²) are the dominant terms of the SEB during the day. Together, they account for at least 70% of the net heat flux into the ground G (see Figure 5). Downwelling LW radiation flux and sensible heat flux are 1 order of magnitude lower than the dominant terms. The moderate atmospheric dust content ($\tau < 1$) and the low atmospheric density ($\sim 10^{-2}$ kg m⁻³) are responsible for the modest role of these two terms in the SEB.

At night, the net surface forcing is negative and it is dominated by surface upwelling LW radiation flux (~ 60 – 100 W/m²) and downwelling LW radiation flux from the atmosphere (~ 50 W/m²). The sensible heat flux is directed toward the surface because temperature inversions occur in the near-surface air. At high wind speeds (~ 10 m/s), the turbulent heat flux is as large as 20 W/m², thus playing a secondary but significant role in the nighttime SEB. The maximum and minimum values of the various terms of the SEB and the times at which they peak are shown in Table 1. Among them, the downwelling LW radiation flux from the atmosphere presents the lowest diurnal variability. It peaks between 1500 and 1600 LMST at each site, which is consistent with the time at which the air temperature measured by REMS peaks.

Potential mechanisms explaining the differences between G and G^* shown in Figure 8 are listed and discussed in section 5. We believe that degradation of the GTS resulting in a loss of sensitivity is the most likely mechanism. Additionally, RTG heating and vertical layering within centimeters of the surface may account for the departures between G and G^* , although we show that these mechanisms are less likely.

On Mars shallow bedrock is usually covered by loose material, such as dust, sand, or regolith. While images can be used to delineate areas of exposed bedrock and surficial materials, they do not unveil the shallow subsurface. Measurements of thermal inertia are capable of unveiling these structures when they are present in the shallow subsurface, providing complementary information about the shallow subsurface not revealed by typical measurements.

Acknowledgments

This research is supported by a grant from JPL 1449038. Germán Martínez wants to thank Harvey Elliott for his contribution to improve this work. We want to thank Hanna Sizemore and the anonymous reviewer for their excellent suggestions to improve the paper. We also thank the REMS Team for their support of this investigation.

References

- Bandfield, J. L., and W. C. Feldman (2008), Martian high latitude permafrost depth and surface cover thermal inertia distributions, *J. Geophys. Res.*, *113*, E08001, doi:10.1029/2007JD008703.
- Blake, D. F., et al. (2013), Curiosity at Gale crater, Mars: Characterization and analysis of the rocknest sand shadow, *Science*, *341*(6153), doi:10.1126/science.1239505.
- Christensen, P. R., et al. (2001), Mars Global Surveyor Thermal Emission Spectrometer experiment: Investigation description and surface science results, *J. Geophys. Res.*, *106*, 23,823–23,871, doi:10.1029/2000JE001370.
- Christensen, P. R., et al. (2004a), Mineralogy at Meridiani Planum from the Mini-TES experiment on the Opportunity rover, *Science*, *306*(5702), 1733–1739.
- Christensen, P. R., et al. (2004b), The Thermal Emission Imaging System (THEMIS) for the Mars 2001 Odyssey mission, *Space Sci. Rev.*, *110*, 85–130.
- Cockell, C. S., and J. A. Raven (2004), Zones of photosynthetic potential on Mars and the early Earth, *Icarus*, *169*(2), 300–310.
- Davy, R., J. A. Davis, P. A. Taylor, C. F. Lange, W. Weng, J. Whiteway, and H. P. Gunnlaugson (2010), Initial analysis of air temperature and related data from the Phoenix met station and their use in estimating turbulent heat fluxes, *J. Geophys. Res.*, *115*, E00E13, doi:10.1029/2009JE003444.
- Edgett, K. S., and P. R. Christensen (1991), The particle size of Martian aeolian dunes, *J. Geophys. Res.*, *96*(E5), 22,765–22,776, doi:10.1029/91JE02412.
- Ferguson, R. L., P. R. Christensen, and H. H. Kieffer (2006a), High-resolution thermal inertia derived from the Thermal Emission Imaging System (THEMIS): Thermal model and applications, *J. Geophys. Res.*, *111*, E12004, doi:10.1029/2006JE002735.
- Ferguson, R. L., P. R. Christensen, J. F. Bell, III, M. P. Golombek, K. E. Herkenhoff, and H. H. Kieffer (2006b), Physical properties of the Mars Exploration Rover landing sites as inferred from Mini-TES-derived thermal inertia, *J. Geophys. Res.*, *111*, E02S21, doi:10.1029/2005JE002583.
- Ferguson, R., P. R. Christensen, M. Golombek, and T. Parker (2012), Surface properties of the Mars Science Laboratory candidate landing sites: Characterization from orbit and predictions, *Space Sci. Rev.*, *170*(1–4), 739–773.
- Golombek, M., et al. (2012), Selection of the Mars Science Laboratory landing site, *Space Sci. Rev.*, *170*(1–4), 641–737.
- Gondet, B., J. Audouard, J.-P. Bibring, Y. Langevin, F. Poulet, and R. Arvidson (2013) OMEGA/Mars Express observations of Gale crater, *Lunar and Planet. Sci.*, *44*, Abstract #2175.
- Gómez-Elvira, J., et al. (2012), REMS: The environmental sensor suite for the Mars Science Laboratory rover, *Space Sci. Rev.*, *170*, 583–640.
- Grotzinger, J., et al. (2012), Mars Science Laboratory mission and science investigation, *Space Sci. Rev.*, *170*, 5–56.
- Grotzinger, J. P., et al. (2013), A habitable fluvio-lacustrine environment at Yellowknife Bay, Gale Crater, Mars, *Science*, *342*, doi:10.1126/science.1242777.
- Haberle, R. M., and B. M. Jakosky (1991), Atmospheric effects on the remote determination of thermal inertia on Mars, *Icarus*, *90*(2), 187–204.
- Haberle, R. M., H. C. Houben, R. Hertenstein, and T. Herdtle (1993), A boundary-layer model for Mars-comparison with Viking lander and entry data, *J. Atmos. Sci.*, *50*, 1544–1559.
- Hamilton, V., et al. (2014), Observations and preliminary science results from the first 100 sols of MSL REMS ground temperature sensor measurements at Gale Crater, *J. Geophys. Res. Planets*, *119*, 745–770, doi:10.1002/2013JE004520.
- Hébrard, E., C. Listowski, P. Coll, B. Marticorena, G. Bergametti, A. Määttänen, F. Montmessin, and F. Forget (2012), An aerodynamic roughness length map derived from extended Martian rock abundance data, *J. Geophys. Res.*, *117*, E04008, doi:10.1029/2011JE003942.
- Kieffer, H. H. (2013), Thermal model for analysis of Mars infrared mapping, *J. Geophys. Res. Planets*, *118*, 451–470, doi:10.1029/2012JE004164.
- Kieffer, H. H., T. Martin, A. R. Peterfreund, B. M. Jakosky, E. D. Miner, and F. D. Palluconi (1977), Thermal and albedo mapping of Mars during the Viking primary mission, *J. Geophys. Res.*, *82*(28), 4249–4291, doi:10.1029/J5082i028p04249.
- Määttänen, A., and H. Savijärvi (2004), Sensitivity tests with a one-dimensional boundary-layer Mars model, *Bound.-Lay. Meteorol.*, *113*(3), 305–320.
- Martínez, G., and N. Rennó (2013), Water and brines on Mars: Current evidence and implications for MSL, *Space Sci. Rev.*, *175*, 29–51.
- Martínez, G., F. Valero, and L. Vázquez (2009), Characterization of the Martian convective boundary layer, *J. Atmos. Sci.*, *66*(7), 2044–2058.
- Martínez, G., F. Valero, and L. Vázquez (2011), The TKE budget in the convective Martian planetary boundary layer, *Q. J. R. Meteorol. Soc.*, *137*(661), 2194–2208.
- Mellon, M. T., B. M. Jakosky, H. H. Kieffer, and P. R. Christensen (2000), High-resolution thermal inertia mapping from the Mars Global Surveyor Thermal Emission Spectrometer, *Icarus*, *148*(2), 437–455.
- Mellon, M. T., W. V. Boynton, W. C. Feldman, R. E. Arvidson, T. N. Titus, J. L. Bandfield, N. E. Putzig, and H. G. Sizemore (2008), A prelanding assessment of the ice-table depth and ground ice characteristics in Martian permafrost at the Phoenix landing site, *J. Geophys. Res.*, *113*, E00A25, doi:10.1029/2007JE003067.
- Möhlmann, D. (2004), Water in the upper Martian surface at mid-and low-latitudes: Presence, state, and consequences, *Icarus*, *168*(2), 318–323.
- Pelkey, S. M., and B. M. Jakosky (2002), Surficial geologic surveys of Gale crater and Melas Chasma, Mars: Integration of remote-sensing data, *Icarus*, *160*(2), 228–257.
- Piqueux, S., and P. R. Christensen (2009a), A model of thermal conductivity for planetary soils: 1. Theory for unconsolidated soils, *J. Geophys. Res.*, *114*, E09005, doi:10.1029/2008JE003308.
- Piqueux, S., and P. R. Christensen (2009b), A model of thermal conductivity for planetary soils: 2. Theory for cemented soils, *J. Geophys. Res.*, *114*, E09006, doi:10.1029/2008JE003309.
- Presley, M. A., and P. R. Christensen (1997), Thermal conductivity measurements of particulate materials 2. Results, *J. Geophys. Res.*, *102*(E3), 6551–6566, doi:10.1029/96JE03303.
- Putzig, N. E., M. T. Mellon, K. A. Kretke, and R. E. Arvidson (2005), Global thermal inertia and surface properties of Mars from the MGS mapping mission, *Icarus*, *173*, 325–341.
- Putzig, N. E., and M. T. Mellon (2007), Apparent thermal inertia and the surface heterogeneity of Mars, *Icarus*, *191*(1), 68–94.

- Savijärvi, H. (1995), Mars boundary layer modeling: Diurnal moisture cycle and soil properties at the Viking lander 1 site, *Icarus*, *117*(1), 120–127.
- Savijärvi, H. (1999), A model study of the atmospheric boundary layer in the Mars Pathfinder lander conditions, *Q. J. R. Meteorol. Soc.*, *125*(554), 483–493.
- Savijärvi, H., and A. Määttänen (2010), Boundary-layer simulations for the Mars Phoenix lander site, *Q. J. R. Meteorol. Soc.*, *136*(651), 1497–1505.
- Savijärvi, H., D. Crisp, and A.-M. Harri (2005), Effects of CO₂ and dust on present-day solar radiation and climate on Mars, *Q. J. R. Meteorol. Soc.*, *131*(611), 2907–2922.
- Sebastián, E., C. Armiens, J. Gómez-Elvira, M. P. Zorzano, J. Martínez-Frías, B. Esteban, and M. Ramos (2010), The rover environmental monitoring station ground temperature sensor: A pyrometer for measuring ground temperature on Mars, *Sensors*, *10*(10), 9211–9231.
- Sinton, W., and J. Strong (1960), Radiometric observations of Mars, *Astrophys. J.*, *131*, 459–469.
- Smith, M. (2004), Interannual variability in TES atmospheric observations of Mars during 1999–2003, *Icarus*, *167*(1), 148–165.
- Smith, M. D., M. J. Wolff, N. Spanovich, A. Ghosh, D. Banfield, P. R. Christensen, G. A. Landis, and S. W. Squyres (2006), One Martian year of atmospheric observations using MER Mini-TES, *J. Geophys. Res.*, *111*, E12S13, doi:10.1029/2006JE002770.
- Squyres, J. W., et al. (2004), In situ evidence for an ancient aqueous environment at Meridiani Panum, Mars, *Science*, *306*, 1709–1714, doi:10.1126/science.1104559.
- Sullivan, R., et al. (2005), Aeolian processes at the Mars Exploration Rover Meridiani Planum landing site, *Nature*, *436*(7047), 58–61.
- Spanovich, N., M. D. Smith, P. H. Smith, M. J. Wolff, P. R. Christensen, and S. W. Squyres (2006), Surface and near-surface atmospheric temperatures from the Mars Exploration Rover landing sites, *Icarus*, *180*, 314–320.
- Spiga, A., F. Forget, J.-B. Madeleine, L. Montabone, S. R. Lewis, and E. Millour (2011), The impact of Martian mesoscale winds on surface temperature and on the determination of thermal inertia, *Icarus*, *212*, 504–519.
- Sutton, J. L., C. B. Leovy, and J. E. Tillman (1978), Diurnal variations of the Martian surface layer meteorological parameters during the first 45 sols at two Viking sites, *J. Atmos. Sci.*, *35*(12), 2346–2355.
- Vasavada, A. R., J. L. Bandfield, B. T. Greenhagen, P. O. Hayne, M. A. Siegler, J. P. Williams, and D. A. Paige (2012), Lunar equatorial surface temperatures and regolith properties from the Diviner Lunar Radiometer Experiment, *J. Geophys. Res.*, *117*, E00H18, doi:10.1029/2011JE003987.
- Zorzano, M., and L. Vázquez (2006), Remote temperature retrieval from heating or cooling targets, *Opt. Lett.*, *31*, 1420–1422.